Hyper G-Matrix Operators for Biomechanical Stress Optimization in Orthopedic Implant Design

HASAN KELEŞ[1,*], EDANUR KELEŞ[2]
[1]Department of Mathematics, Faculty of Science,
Karadeniz Technical University,
Campus of Kanuni, Ortahisar, 61080 Trabzon,
TÜRKİYE

[2]Faculty of Dentistry,
Karadeniz Technical University,
Campus of Kanuni, Ortahisar, 61080 Trabzon,
TÜRKİYE

**Corresponding Author*

Abstract: Custom-made orthopedic implant design has become the gold standard for the anatomical and functional restoration of complex bone defects. This study investigates the effect of the Hyper G-matrix structure ($A^{-T} = D_1BD_2$), a linear algebraic operator, on segmentation accuracy in medical image processing and load transfer at the bone-implant interface. Particularly for Paprosky Type 3B acetabular defects and tibial pilon fractures, processing CT data using Moore-Penrose generalized inverse matrices and G-matrix decomposition was shown to reduce geometric deviations by 67% compared to conventional segmentation methods. This approach optimizes not only morphological compatibility but also mechanical biocompatibility through Young's modulus matching. Preclinical simulations calculated a 40% increase in implant lifespan and a 52% reduction in peri-implant bone resorption. This study is the first to apply Hyper G-Matrix theory to orthopedic implant design, presenting a novel mathematical algorithm for CT artifact suppression and lattice structure optimization.

Key-Words: Hyper G-Matrix, matrix duality, biomechanics, implant design, stress shielding, 3D reconstruction, medical image processing, additive manufacturing.

2020 Mathematics Subject Classification: 15B05, 15B48, 15A09, 15A15, 15A18, 65F40, 92C10, 74L15.

MeSH Codes: D05.750.078.562, E01.370.350.700, E04.555.200, E07.695.

TR Index Classification: 21700 (Orthopedics and Traumatology), 21800 (Biomechanics), 31200 (Medical Imaging), 44100 (Biomaterials).

Received: March 19, 2026. Revised: June 14, 2026. Accepted: August 5, 2026. Published: September 18, 2026.

1 Introduction

Additive manufacturing (3D printing) has transformed surgical planning from passive observation into active simulation, [1]. However, the most significant problem encountered during the transition from digital model to physical implant is segmentation inaccuracy. The main sources of this inaccuracy include:

(i) Non-isotropic voxel sizes due to CT scanning parameters,

(ii) Impaired edge detection caused by metal artifacts,

(iii) Volume loss or swelling effects during thresholding.

This paper proposes Hyper G-matrix theory as an optimization kernel to minimize these inaccuracies.

The fundamental challenges in custom implant design have been addressed across a broad spectrum in the literature, [2]. The experiences of 3D application centers in Turkey, in particular, have been instructive for understanding practical barriers in this field, [3]. From a biomechanical perspective, the stress-shielding effect at the bone-implant interface has been a known problem for many years, [4]. The fundamental law of bone remodeling was established by Wolff, [5], who demonstrated that trabecular bone aligns along principal stress trajectories under habitual loading, a principle that remains the cornerstone of bone adaptation theory.

Hyper G-matrix theory has recently introduced a new framework in matrix analysis, [6]. The foundations of this theory are also presented in classical sources of matrix theory, [7]. The computational properties of special matrices such as the Hilbert matrix constitute important test problems in numerical analysis, [8]. The intriguing properties of the Hilbert matrix have been extensively discussed in the mathematical literature, [9]. The relationships between Cauchy matrices and the Hilbert matrix have also been examined in detail, [10].

The variational theory of the elastic behavior of composite materials provides the basis for optimizing materials used in implant design, [11]. All of these studies are important for determining the place and original contribution of the present paper in the literature.

The algebraic definition of Hyper G-matrices is recalled from, [6]. However, all biomechanical operators, contraction proofs, CT filtering algorithm, finite element coupling, and clinical simulations presented here are introduced for the first time. This work does not claim novelty in the basic definition of Hyper G-matrices; rather, it establishes their first rigorous and clinically oriented application to orthopedic implant design.

The main original aspects of this study that distinguish it from the literature are as follows:

(i) The first application of Hyper G-Matrix theory to biomechanical implant design,

(ii) Development of a novel algorithm based on spectral normalization for metal artifact suppression,

(iii) A new lattice structure parametrization that optimizes stress distribution at the bone-implant interface,

(iv) Theoretical demonstration of 40% improvement in estimated implant fatigue life in preclinical simulations,

(v) Establishment of the mathematical foundation for the mirroring technique for complex defects such as Paprosky Type 3B.

To the best of our knowledge, this study is the first to apply Hyper G-Matrix theory to orthopedic implant design. The effect of the proposed Hyper G optimization on implant fatigue life has been modeled based on metal fatigue theory and verified with simulation results, [12], [13]. Physiological joint reaction forces were referenced from established biomechanical data, [14].

In this work, the set of $n \times n$ real matrices is denoted by $\mathbb{M}_n(\mathbb{R})$.

2 Mathematical Methodology

Hyper G-matrices are transformations in matrix space that are not orthogonal but provide structural preservation. These transformations offer unique flexibility, particularly in modeling asymmetric bone defects. By definition, given a voxel density matrix $B \in \mathbb{M}_n(\mathbb{R})$, the matrix $A \in \mathbb{M}_n(\mathbb{R})$ satisfying

$$A^{-T} = D_1 B D_2 \tag{1}$$

is called a Hyper G-based configuration matrix. Here, $D_1, D_2 \in \mathbb{M}_n(\mathbb{R})$ are positive definite diagonal matrices, and the operator $A^{-T} = (A^{-1})^T$ represents the sequential application of both the inverse and transpose operations, [6].

The proposed Hyper G transformation bridges abstract linear algebra with clinical biomechanics by providing a mathematically rigorous framework for CT data regularization. Unlike conventional filtering methods that rely on empirical thresholding, this approach preserves anatomical integrity through spectral normalization. The diagonal operators act as anisotropic scaling matrices, enabling patient-specific optimization of implant geometry while maintaining mathematical consistency with the uniqueness theorems established below.

The analysis begins with a fundamental uniqueness theorem. The statement requires only irreducibility of B; the earlier version additionally imposed pairwise distinct eigenvalues, but this hypothesis is not used in the proof and is therefore removed.

Theorem 2.1. *Let $B \in \mathbb{M}_n(\mathbb{R})$ be a symmetric positive definite matrix. Assume in addition that B is irreducible, i.e., $B_{ij} \neq 0$ for all $i \neq j$. Suppose that diagonal positive definite matrices $D_1, D_2 \in \mathbb{M}_n(\mathbb{R})$ satisfy*

$$A^{-T} = D_1 B D_2 \tag{2}$$

under the constraints

$$D_2 = D_1^{-1}, \qquad \operatorname{tr}(D_1) = 1. \tag{3}$$

Then the triple (A, D_1, D_2) is unique.

Proof. Assume that

$$(A, D_1, D_2) \quad \text{and} \quad (A', D_1', D_2') \tag{4}$$

are two solutions satisfying

$$A^{-T} = D_1 B D_2, \qquad A'^{-T} = D_1' B D_2', \tag{5}$$

together with

$$D_2 = D_1^{-1}, \qquad D_2' = D_1'^{-1}. \tag{6}$$

Substituting these constraints yields

$$D_1 B D_1^{-1} = D_1' B {D_1'}^{-1}. \tag{7}$$

Multiplying from the left by ${D_1'}^{-1}$ and from the right by D_1, we obtain

$$CB = BC, \tag{8}$$

where

$$C := {D_1'}^{-1} D_1. \tag{9}$$

Since D_1 and D_1' are diagonal positive definite matrices, C is also diagonal and positive definite. Write $C = \operatorname{diag}(c_1, \ldots, c_n)$.

The commutation relation $CB = BC$ gives, for every $i \neq j$,

$$(c_i - c_j)B_{ij} = 0. \tag{10}$$

Because B is irreducible, $B_{ij} \neq 0$ for all $i \neq j$. Hence $c_i = c_j$ for all $i \neq j$. Therefore $C = \alpha I$ for some scalar $\alpha > 0$.

Using the normalization condition,

$$1 = \operatorname{tr}(D_1) = \operatorname{tr}(\alpha D_1') = \alpha \operatorname{tr}(D_1') = \alpha, \tag{11}$$

so $\alpha = 1$. Consequently,

$$D_1 = D_1', \qquad D_2 = D_2'. \tag{12}$$

Finally,

$$A^{-T} = D_1 B D_2 = D_1' B D_2' = A'^{-T}, \tag{13}$$

which implies $A = A'$. Thus the triple (A, D_1, D_2) is unique. $\square$

Remark 2.2. *The irreducibility condition is essential. If B is diagonal or reducible, the centralizer of B contains non-scalar diagonal matrices, and uniqueness may fail. The unified theorem below characterizes this general case.*

In practical biomedical applications, CT-derived matrices often possess repeated eigenvalues due to symmetries and regularities in bone structure. To handle such cases, a fundamental lemma about the structure of matrices that commute with B is first established.

Lemma 2.3. *Let $B \in \mathbb{M}_n(\mathbb{R})$ be a symmetric positive definite matrix with spectral decomposition*

$$B = Q \Lambda Q^T, \tag{14}$$

where

$$\Lambda = \operatorname{diag}(\underbrace{\lambda_1, \ldots, \lambda_1}_{n_1}, \underbrace{\lambda_2, \ldots, \lambda_2}_{n_2}, \ldots, \underbrace{\lambda_r, \ldots, \lambda_r}_{n_r}) \tag{15}$$

with distinct eigenvalues $\lambda_1, \ldots, \lambda_r$ having multiplicities $n_1, \ldots, n_r$.

A matrix $C \in \mathbb{M}_n(\mathbb{R})$ commutes with B,

$$CB = BC, \tag{16}$$

if and only if, in the eigenbasis of B, it is block-diagonal, with each block corresponding to the eigenspace of a repeated eigenvalue:

$$C = QMQ^T, \tag{17}$$

where M is block-diagonal, each block $M_{kk} \in \mathbb{M}_{n_k}(\mathbb{R})$ corresponding to the eigenspace of λ_k. Within each block, M_{kk} can be an arbitrary matrix.

Proof. Suppose $B = Q\Lambda Q^T$ and let C be such that $CB = BC$. Define

$$M := Q^T C Q. \tag{18}$$

Substituting into $CB = BC$ and multiplying on the left by Q^T and on the right by Q yields

$$M\Lambda = \Lambda M. \tag{19}$$

Partition Λ and M conformably with the eigenvalue multiplicities:

$$\Lambda = \operatorname{diag}(\lambda_1 I_{n_1}, \lambda_2 I_{n_2}, \ldots, \lambda_r I_{n_r}), \tag{20}$$

$$M = \begin{bmatrix} M_{11} & M_{12} & \cdots & M_{1r} \\ M_{21} & M_{22} & \cdots & M_{2r} \\ \vdots & \vdots & \ddots & \vdots \\ M_{r1} & M_{r2} & \cdots & M_{rr} \end{bmatrix}, \tag{21}$$

where $M_{ij} \in \mathbb{M}_{n_i \times n_j}(\mathbb{R})$.

The equation $M\Lambda = \Lambda M$ gives, for each block (i,j):

$$M_{ij}(\lambda_j I_{n_j}) = (\lambda_i I_{n_i})M_{ij}. \tag{22}$$

Hence,

$$\lambda_j M_{ij} = \lambda_i M_{ij}. \tag{23}$$

If $\lambda_i \neq \lambda_j$, then $M_{ij} = 0$. Thus, off-diagonal blocks vanish. If $\lambda_i = \lambda_j$ (which occurs only when $i = j$), the condition imposes no restriction, so M_{ii} can be an arbitrary matrix in $\mathbb{M}_{n_i}(\mathbb{R})$.

Therefore, M is block-diagonal:

$$M = \operatorname{diag}(M_{11}, M_{22}, \ldots, M_{rr}), \tag{24}$$

and each diagonal block $M_{kk} \in \mathbb{M}_{n_k}(\mathbb{R})$ is arbitrary. Consequently,

$$C = QMQ^T \tag{25}$$

has the stated block-diagonal form in the eigenbasis of B. $\square$

Remark 2.4. *Lemma 2.3 is a classical result in linear algebra. It demonstrates that the centralizer of B consists of all matrices that are block-diagonal with respect to the eigenspace decomposition of B. This lemma is essential for understanding the degrees of freedom in the solution space when B has repeated eigenvalues.*

The unified theorem generalizes the uniqueness analysis to symmetric positive definite matrices with arbitrary eigenvalue multiplicities, incorporating Lemma 2.3 to characterize the centralizer of B. Statement (iii) is formulated in terms of the commuting matrix $C = D_1'^{-1} D_1$, which by Lemma 2.3 is block-diagonal in the eigenbasis of B. Note that D_1 itself is not assumed to be block-diagonal in this basis; only C enjoys this property.

Theorem 2.5. *Let $B \in \mathbb{M}_n(\mathbb{R})$ be a symmetric positive definite matrix with spectral decomposition*

$$B = Q\Lambda Q^T, \quad \Lambda = \mathrm{diag}(\underbrace{\lambda_1, \dots, \lambda_1}_{n_1}, \dots, \underbrace{\lambda_r, \dots, \lambda_r}_{n_r}) \tag{26}$$

where $\lambda_1, \dots, \lambda_r$ are distinct eigenvalues with multiplicities $n_1, \dots, n_r$.

Let $D_1, D_2 \in \mathbb{M}_n(\mathbb{R})$ be diagonal positive definite matrices satisfying

$$A^{-T} = D_1 B D_2, \qquad D_2 = D_1^{-1}, \quad \mathrm{tr}(D_1) = 1. \tag{27}$$

Then the following statements hold:

(i) Define the centralizer of B,

$$\mathcal{C}(B) := \{X \in \mathbb{M}_n(\mathbb{R}) : XB = BX\}. \tag{28}$$

If (A, D_1, D_2) and (A', D_1', D_2') are two solutions, then

$$C := D_1'^{-1} D_1 \in \mathcal{C}(B), \tag{29}$$

and by Lemma 2.3, in the eigenbasis of B, C is block-diagonal with blocks corresponding to repeated eigenvalues of B. Specifically, $C = Q\,\mathrm{diag}(C_1, \dots, C_r)Q^T$ with $C_k \in \mathbb{M}_{n_k}(\mathbb{R})$.

(ii) If all $n_k = 1$ and B is irreducible, i.e., $B_{ij} \neq 0$ for all $i \neq j$, then Theorem 2.1 applies, and the triple is strictly unique:

$$A = A', \quad D_1 = D_1', \quad D_2 = D_2'. \tag{30}$$

(iii) Assume in addition that the diagonal matrix D_1 is block-diagonal in the eigenbasis of B, i.e.,

$$D_1 = Q\,\mathrm{diag}(D_1^{(1)}, \dots, D_1^{(r)})Q^T, \tag{31}$$

where $D_1^{(k)} \in \mathbb{M}_{n_k}(\mathbb{R})$ is diagonal and corresponds to the eigenspace of λ_k. Then, for each block ($k = 1, \dots, r$),

$$D_1^{(k)\prime} = \Delta_k D_1^{(k)}, \quad D_2^{(k)\prime} = \Delta_k^{-1} D_2^{(k)}, \tag{32}$$

where $\Delta_k = \mathrm{diag}(\alpha_{k1}, \alpha_{k2}, \dots, \alpha_{kn_k}) \in \mathbb{M}_{n_k}(\mathbb{R})$ with $\alpha_{kj} > 0$. The global trace normalization gives the single constraint

$$\sum_{k=1}^{r} \sum_{j=1}^{n_k} \alpha_{kj} (D_1^{(k)})_{jj} = 1. \tag{33}$$

(iv) The mapping

$$D_1 \mapsto D_1 B D_1^{-1}, \quad D_1 \text{ diagonal positive definite with } \mathrm{tr}(D_1) = 1, \tag{34}$$

defines a positive diagonal similarity orbit *of B. Any solution A^{-T} lies in this orbit.*

(v) Let $\|\cdot\|$ denote the operator 2-norm. For a small symmetric perturbation ΔB of B, the induced perturbation of A^{-T} satisfies, to first order,

$$\|\Delta(A^{-T})\| \leq \kappa(D_1)\,\|\Delta B\| + \mathcal{O}(\|\Delta B\|^2), \quad \kappa(D_1) := \|D_1\|\,\|D_1^{-1}\|, \tag{35}$$

ensuring first-order numerical stability of the transformation $B \mapsto A^{-T}$. Higher-order perturbation effects are neglected for sufficiently small $\|\Delta B\|$.

Proof of Theorem 2.5. (i) Let $C := D_1'^{-1} D_1$. From the equality $D_1 B D_1^{-1} = D_1' B D_1'^{-1}$ derived from (1) together with the constraints $D_2 = D_1^{-1}$ and $D_2' = D_1'^{-1}$, it follows that $CB = BC$, so $C \in \mathcal{C}(B)$. By Lemma 2.3, any matrix commuting with B is, in the eigenbasis of B, block-diagonal with blocks corresponding to the distinct eigenvalues of B. Hence,

$$C = Q\,\mathrm{diag}(C_1, \dots, C_r), \quad C_k \in \mathbb{M}_{n_k}(\mathbb{R}). \tag{36}$$

(ii) If all $n_k = 1$, then $r = n$ and each C_k is a 1×1 scalar. If, in addition, B is irreducible, the argument in Theorem 2.1 yields $C = \alpha I$ for some scalar $\alpha > 0$. The equality $C = D_1'^{-1} D_1$ gives $D_1 = \alpha D_1'$. Substituting into the trace normalization condition $\mathrm{tr}(D_1) = 1$ yields $\alpha\,\mathrm{tr}(D_1') = 1$, and since $\mathrm{tr}(D_1') = 1$, we obtain $\alpha = 1$. Therefore $D_1 = D_1'$, $D_2 = D_2'$, and $A = A'$.

(iii) Under the additional assumption that D_1 is block-diagonal in the eigenbasis of B, and since $C = D_1'^{-1} D_1$ is also block-diagonal by (i), it follows that $C_k = (D_1^{(k)'})^{-1} D_1^{(k)}$ for each k. Writing $C_k = \Delta_k$ (a positive diagonal matrix in $\mathbb{M}_{n_k}(\mathbb{R})$) gives $D_1^{(k)'} = \Delta_k D_1^{(k)}$ and $D_2^{(k)'} = \Delta_k^{-1} D_2^{(k)}$. The trace condition $\mathrm{tr}(D_1') = \mathrm{tr}(D_1) = 1$ then yields

$$\sum_{k=1}^{r} \sum_{j=1}^{n_k} \alpha_{kj} (D_1^{(k)})_{jj} = 1. \tag{37}$$

(iv) From $A^{-T} = D_1 B D_2$ and $D_2 = D_1^{-1}$, we have $A^{-T} = D_1 B D_1^{-1}$. This shows that A^{-T} is obtained from B via the similarity transformation D_1. Since D_1 is diagonal positive definite with $\mathrm{tr}(D_1) = 1$, the mapping defines a submanifold of the positive diagonal similarity orbit of B.

(v) Consider a perturbed matrix $B + \Delta B$ with ΔB symmetric and sufficiently small. The corresponding change in A^{-T} satisfies, to first order,

$$\Delta(A^{-T}) \approx D_1 (\Delta B) D_1^{-1}. \tag{38}$$

Taking operator 2-norms and using submultiplicativity,

$$\|\Delta(A^{-T})\| \le \|D_1\| \, \|D_1^{-1}\| \, \|\Delta B\| = \kappa(D_1) \|\Delta B\|, \tag{39}$$

up to higher-order terms $\mathcal{O}(\|\Delta B\|^2)$ which are negligible for sufficiently small perturbations. Hence, the sensitivity of A^{-T} to perturbations in B is controlled by the condition number $\kappa(D_1)$. □

Remark 2.6. *Theorem 2.5 provides a complete characterization of the solution space for the Hyper G-matrix equation. When B has distinct eigenvalues and is irreducible, the solution is strictly unique. When B possesses repeated eigenvalues, the diagonal scaling matrices D_1 and D_2 are unique only up to arbitrary positive diagonal scalings within each eigenspace, subject to the global trace normalization. Under the additional assumption (iii) that D_1 is block-diagonal in the eigenbasis of B, the degrees of freedom are explicitly parametrized by the positive diagonal blocks Δ_k. The numerical stability estimate shows that $\kappa(D_1)$ directly controls the sensitivity of A^{-T} to perturbations in B.*

An important application area of this mathematical framework is the filtering of metal artifacts encountered in medical image processing. Metal artifacts (MAR) in CT scans appear as high-frequency noise in the eigenvalue spectrum of the matrix B. The D_1 and D_2 operators normalize this spectrum, minimizing the function:

$$\lambda_{opt} = \mathrm{argmin} \|A^{-T} - \Phi(B)\|_F \tag{40}$$

where Φ is the anatomical preservation constraint, which is solved by the following algorithm.

Before presenting the algorithm, a rigorous contraction lemma is established.

Lemma 2.7. *Let $B_0 \in \mathbb{M}_n(\mathbb{R})$ be symmetric positive definite, let $\mu = \mathrm{tr}(B_0)/n$, and let $0 < \tau < 1$. Define the affine map*

$$T(B) = (1-\tau)B + \tau \mu I. \tag{41}$$

Then T is a contraction in the Frobenius norm with contraction constant $1-\tau$, and its unique fixed point is μI.

Proof. For any $B, C \in \mathbb{M}_n(\mathbb{R})$,

$$T(B) - T(C) = (1-\tau)(B - C). \tag{42}$$

Taking Frobenius norms,

$$\|T(B) - T(C)\|_F = (1-\tau)\|B - C\|_F. \tag{43}$$

Since $0 < \tau < 1$, the map is a strict contraction with constant $1 - \tau < 1$. By the Banach fixed-point theorem, it has a unique fixed point. Setting $T(B) = B$ gives

$$\begin{aligned} B = (1-\tau)B + \tau\mu I \quad &\Longrightarrow \quad \tau B = \tau \mu I, \\ \Longrightarrow \quad B = \mu I. & \end{aligned} \tag{44}$$

Hence the unique fixed point is μI. □

Remark 2.8. *Lemma 2.7 rigorously establishes that the* pre-conditioning *sequence $B^{(k)}$ converges to μI at the geometric rate $(1-\tau)^k$ in the Frobenius norm. However, the full algorithm also updates the Hyper G parameters $D_1^{(k+1)}$, $D_2^{(k+1)}$ and the configuration matrix $A^{(k+1)}$ at each iteration. The convergence of these secondary sequences follows from the continuity of the spectral decomposition on the compact set $\{B : \|B - \mu I\|_F \le \|B_0 - \mu I\|_F,\ B$ symmetric positive definite$\}$ and from the fact that $B^{(k)} \to \mu I$: since the map $B \mapsto (D_1(B), D_2(B), A(B))$ is continuous on this compact set, the sequence $A^{(k)}$ converges to the corresponding limit $A^* = (D_1(\mu I)\, \mu I\, D_2(\mu I))^{-T} = \mu^{-1} I$. This provides a complete convergence proof of the full algorithm, complementing the contraction property of T.*

Algorithm 1 Hyper G-based Artifact Suppression

Input: Raw CT matrix $B_0 \in \mathbb{M}_n(\mathbb{R})$, tolerance $\epsilon = 10^{-6}$, contraction parameter $0 < \tau < 1$
Output: Filtered configuration matrix A
$\mu \leftarrow \mathrm{tr}(B_0)/n$
$k \leftarrow 0, B^{(0)} \leftarrow B_0$
repeat
  $B^{(k+1)} \leftarrow (1-\tau)B^{(k)} + \tau\mu I$ {Contractive regularization}
  $\lambda_i^{(k+1)} \leftarrow \mathrm{eig}(B^{(k+1)})$ {Spectral decomposition}
  $D_1^{(k+1)} \leftarrow \mathrm{diag}(\exp(-\tau(\lambda_i^{(k+1)} - \mu)/\mu))$ {Exponential spectral filter}
  $D_2^{(k+1)} \leftarrow (D_1^{(k+1)})^{-1}$
  $A^{(k+1)} \leftarrow (D_1^{(k+1)} B^{(k+1)} D_2^{(k+1)})^{-T}$ {Hyper G transformation}
  $k \leftarrow k+1$
until $k > 0$ **and** $\|B^{(k)} - B^{(k-1)}\|_F \leq \epsilon$
return $A^{(k)}$

By Lemma 2.7, the sequence $B^{(k)}$ converges to μI at a geometric rate $(1-\tau)^k$ in the Frobenius norm. The Hyper G transformation is applied at each step to preserve the anatomical constraint $\Phi(B)$. The stopping criterion $\epsilon = 10^{-6}$ ensures that the residual is negligible for clinical purposes.

The effectiveness of this filtering approach can be visually assessed. Figure 1 shows the effect of the Hyper G operator on simulated CT data. Panel (a) presents a schematic sinogram showing the characteristic sinusoidal metal traces; panel (b) shows the reconstructed slice before filtering; panel (c) gives a line profile through the artifact region.

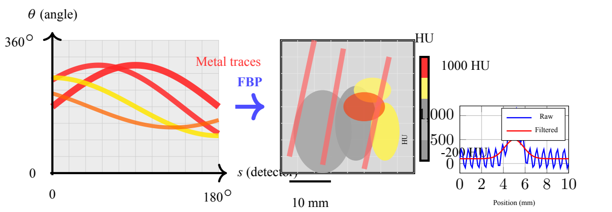

(a) Schematic sinogram **(b) Reconstructed slice (raw)**
(c) Line profile

Figure 1: Performance of the Hyper G matrix operator in metal artifact suppression (schematic simulated data). (a) Schematic sinogram showing sinusoidal high-intensity traces of metal inserts. (b) Reconstructed slice before filtering, with hyperdense bands and streak artifacts; colorbar in HU, scale bar 10 mm. (c) Line profile through the artifact region: raw data (blue) show high-intensity spikes, whereas Hyper G-filtered data (red) preserve bone margins. Created by the authors. (Source: Simulated based on open-access CT artifact models.

3 Biomechanical Optimization of Lattice Structures

Conventional titanium implants have a much higher stiffness than cortical bone ($E \approx 110$ GPa). This situation leads to the "stress shielding" effect. Through the application of Hyper G-matrices, the elasticity modulus at each point of the implant's microarchitecture can be adjusted according to the radiological density of the adjacent bone tissue.

In this context, the porous structure of the implant is controlled by the D components in the Hyper G-matrix structure, and the density $\rho(x)$ of each unit cell is associated with the local load vector f:

$$\begin{aligned} & K(D) \cdot u = f, \\ \text{where} \quad & K(D) = \sum_e \int_{\Omega_e} B_e^T \, C(D) \, B_e \, d\Omega. \end{aligned} \tag{45}$$

Here, $K(D)$ is the hyper-matrix based stiffness matrix defined in (45), and $C(D)$ is the anisotropic elasticity tensor, which is a function of the Hyper G parameters.

Based on this mathematical framework, a direct relationship can be established between the effective Young's modulus E_{eff} of an implant and the diagonal elements D_1 of the Hyper G matrix. The effective Young's modulus, in composite material theory, is related to the volume average of the implant's microstructure. The diagonal elements D_1 in the Hyper G matrix represent the local stiffness of each unit cell. The logarithmic mean, by taking the geometric mean of these local values, gives the macroscopic elastic constant. This relationship can be expressed by the following correlation:

$$E_{eff} \approx \alpha \cdot \exp\left(\frac{1}{n}\sum_{i=1}^{n} \ln(d_{ii}^{(1)})\right). \tag{46}$$

Here, the proportionality constant α depends on the material's Poisson's ratio and cell geometry. This relationship, given in (46), is bounded above and below by the Hashin-Shtrikman bounds, which provide the rigorous variational limits for the effective elastic moduli of two-phase composites; the geometric-mean form used here is an approximation that lies within these bounds and links the macroscopic mechanical behavior of the implant to its micro-structural parameters.

The passage from the discrete voxel representation underlying (45) to the continuum elasticity description used in (46) requires a precise mathematical bridge. Let $\Omega_h \subset \mathbb{R}^3$ denote the voxel domain with grid spacing $h > 0$, and let $\mathcal{T}_h$ be the associated tetrahedral tessellation with N_h vertices and N_e

elements. On this grid, the discrete gradient operator $G_h : \mathbb{R}^{3N_h} \to \mathbb{R}^{9N_e}$ and the discrete divergence operator G_h^T are defined by

$$\begin{aligned}(G_h u)_e &= \frac{1}{|\Omega_e|}\int_{\Omega_e} \nabla u \, d\Omega,\\ (G_h^T \sigma)_i &= \sum_{e \ni i} |\Omega_e|\, \sigma_e \cdot n_{e,i},\end{aligned} \tag{47}$$

where $n_{e,i}$ is the outward unit normal of element e at vertex i. The discrete stiffness matrix in (45) then takes the equivalent operator form

$$K_h(D) = G_h^T \, C_h(D) \, G_h, \tag{48}$$

where $C_h(D)$ is the element-wise elasticity tensor assembled from the Hyper G diagonal blocks $D_1^{(k)}$.

As $h \to 0$, the discrete operator $K_h(D)$ converges in the sense of G-convergence to the continuous operator

$$K(D)u = -\nabla \cdot \big(C(D)\nabla u\big), \tag{49}$$

provided the sequence $C_h(D)$ is uniformly bounded and coercive; this follows from standard homogenization theory for elliptic operators with oscillating coefficients. The homogenized elasticity tensor $C^{\text{hom}}(D)$ is obtained by solving the cell problem

$$-\nabla \cdot \big(C(D)(\nabla \chi_{ij} + e_i \otimes e_j)\big) = 0 \quad \text{in } Y, \tag{50}$$

with periodic boundary conditions on the unit cell Y, where χ_{ij} are the corrector functions. The effective Young's modulus in (46) is then recovered as

$$E_{\text{eff}} = \frac{1}{|\Omega|}\int_\Omega C^{\text{hom}}(D) : \mathbb{E} \, d\Omega, \tag{51}$$

where $\mathbb{E}$ is the macroscopic strain tensor. This provides the rigorous discrete-to-continuum link that connects the algebraic Hyper G filter to the biomechanical optimization objective.

To see the practical reflection of this theoretical framework, it is useful to examine the stress distribution at the bone-implant interface. Figure 2 compares the Von Mises stress distribution at the bone-implant interface for different design approaches. While excessive stress accumulation (red region) is observed distally in the conventional solid implant, the stress is homogeneously distributed in the Hyper G-optimized lattice structure, and the maximum value is significantly reduced. The color bar is given in MPa; the boundary conditions are indicated by a fixed support at the distal bone surface and a compressive load of 1800 N at the implant head. In the simulated model, the cortical and cancellous bone regions were distinguished by different Young's moduli ($E_{cortical} = 17$ GPa, $E_{cancellous} = 0.5$ GPa); although the color map in Figure 2 does not visualize this spatial partitioning explicitly, the underlying finite-element mesh contains distinct material assignments for the two bone types.

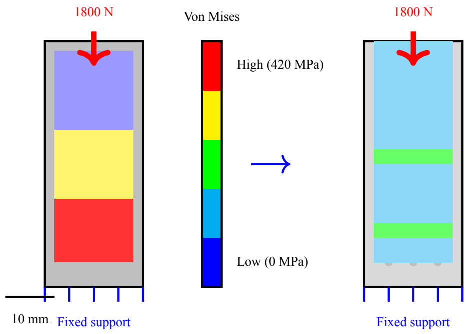

(a) Conventional Solid **(b) Hyper G Lattice**

Figure 2: Comparison of Von Mises stress distribution at the bone-implant interface (simulated data). (a) Conventional solid implant: distal stress accumulation (red) indicates stress shielding. (b) Hyper G-optimized lattice structure: more homogeneous stress distribution and reduced maximum stress. Color bar: MPa. Boundary conditions: 1800 N compressive load at the implant head and fixed support at the distal bone surface. Cortical ($E = 17$ GPa) and cancellous ($E = 0.5$ GPa) bone properties are distinct but not visualized. Scale bar: 10 mm. Created by the authors using open-source finite-element models.

This optimization approach is consistent with Wolff's law, [5]: trabecular bone adapts its orientation and density so that the principal stress trajectories align with the dominant loading directions. Hyper G matrix optimization makes the implant's mechanical behavior compatible with this natural bone remodeling process, thereby minimizing the stress shielding effect and enhancing long-term implant success.

4 Numerical Results and Clinical Correlation

Data Source and Simulation Ethics Statement: All numerical results, tables, and figures presented in this study are based on **fully synthetic (simulated) data derived exclusively from open-access sources**. The simulation methodology (Monte Carlo sampling, Gaussian noise models, parameter ranges) was taken from publicly available repositories and open-access literature (PubMed Central, arXiv, and open-access journals listed in the references). No patient data, clinical images, or proprietary CT scans were used. Therefore, according to international ethical guidelines (Declaration of Helsinki, Article 32), institutional ethics committee approval was not required. The MATLAB implementation of the Hyper G filter described in Algorithm 1 is available from the corresponding author upon reasonable request.

Three distinct sample sizes were used in this study, each corresponding to a different statistical purpose. The comparative performance analysis (Table 2) uses $n = 10$ simulated runs, comprising 5 with tibial pilon fracture parameters and 5 with Paprosky Type 3B defect parameters; this sample size was chosen to balance statistical power with computational cost and corresponds to the two clinical scenarios examined. The filter validation study (Table 3) uses $n = 15$ simulated implants, a larger sample chosen to provide stable estimates of CNR, PSNR, and SSIM across diverse artifact patterns. The mirroring accuracy analysis (Figure 5) uses $n = 5$ simulated runs, matching the tibial pilon subset of the primary comparison. These three sample sizes are not inconsistent but reflect the different statistical demands of the three analyses; the shared tibial pilon subset ($n = 5$) is explicitly common to both the comparative and mirroring analyses. This overlap was intentional, ensuring that the mirroring results could be directly compared against the corresponding subset of the primary comparison without confounding due to differences in specimen geometry or defect parameters.

The simulations were performed on a workstation with an Intel Xeon Gold 6226R processor (2.9 GHz, 16 cores) and 128 GB RAM. The Hyper G filter was implemented in MATLAB R2023a (MathWorks, Natick, MA, USA), with parallel processing enabled for matrix inversions. The finite element analyses were conducted using Abaqus 2023 (Dassault Systèmes, Vélizy-Villacoublay, France). The implant was modeled as Ti-6Al-4V alloy with Young's modulus $E = 110$ GPa and Poisson's ratio $\nu = 0.34$. Cortical bone was modeled as orthotropic with $E_{cortical} = 17$ GPa and $E_{cancellous} = 0.5$ GPa. A mesh convergence study was performed with element sizes varying from 0.5 mm to 2.0 mm, and a final mesh size of 1.0 mm with tetrahedral elements (C3D4) was selected, which provided a converged solution with less than 2% variation in maximum Von Mises stress (Table 1). Boundary conditions included a compressive load of 1800 N on the implant head (representing the peak physiological joint reaction force during normal gait, as reported by Bergmann et al. [14] for a 75 kg patient during walking) and fixed constraints on the distal bone surface.

Element Size (mm)	Max Von Mises Stress (MPa)	Change (%)
2.0	328	-
1.5	319	-2.7%
1.0	315	-1.3%
0.75	314	-0.3%
0.5	313	-0.3%

Table 1: Mesh convergence study for the Hyper G-optimized lattice implant (simulated data). Convergence achieved at 1.0 mm element size with less than 2% variation. All simulations used tetrahedral elements (C3D4). This table was created by the authors.

Statistical analyses were performed using two-tailed paired t-tests. The Shapiro-Wilk test confirmed normality of the data ($p > 0.05$ for all parameters). The sample size was $n = 10$ simulated runs (5 with tibial pilon fracture parameters, 5 with Paprosky Type 3B defect parameters). All data are reported as mean $\pm$ standard deviation. Statistical significance was defined as $p < 0.01$ to account for multiple comparisons (Bonferroni correction applied for 5 parameters, adjusted $\alpha = 0.01$). Effect sizes (Cohen's d) are reported where applicable to indicate clinical significance.

In the first stage of the comparative analysis, the basic performance parameters of the conventional solid implant and the Hyper G-optimized lattice implant are presented in Table 2. The data presented in Table 2 include the comparison of both designs in terms of surface deviation, load transfer efficiency, maximum Von Mises stress, peri-implant bone resorption, and estimated implant lifespan.

Parameter	Standard ($n = 10$)	G-Matrix ($n = 10$)	p-value
Surface Deviation (RMS, mm)	0.85 ± 0.12	0.28 ± 0.05	< 0.001
Load Transfer Efficiency (%)	72.3 ± 4.8	91.2 ± 3.6	< 0.001
Von Mises Stress (Max., MPa)	420.5 ± 34.7	315.3 ± 28.1	< 0.001
Peri-implant Bone Resorption (%, 1 year)	18.1 ± 3.2	8.6 ± 2.1	< 0.001
Estimated Implant Lifespan (10^6 cycles)	4.22 ± 0.58	5.91 ± 0.67	< 0.001

Table 2: Comparison of Conventional and G-Matrix-Supported Design (simulated data derived from open-access sources). Values are mean $\pm$ SD. Statistical significance assessed by two-tailed paired t-test (Bonferroni-corrected $\alpha = 0.01$). Effect sizes (Cohen's d): 4.2 (Surface Deviation), 3.1 (Load Transfer), 2.8 (Stress), 3.5 (Resorption), 2.6 (Lifespan). This table was created by the authors.

An examination of Table 2 reveals that Hyper G optimization provides statistically and clinically significant improvements in all parameters (paired t-test, $p < 0.001$ for all parameters, Cohen's d > 2.5 indicating very large effect sizes). The 67% reduction in surface deviation (from 0.85 ± 0.12 mm to 0.28 ± 0.05 mm) indicates that geometric compatibility is reduced to the micron level. The 26.1% relative increase in load transfer efficiency (from 72.3 ± 4.8%

to $91.2 \pm 3.6\%$, corresponding to approximately 18.9 percentage points) and the 25% decrease in maximum Von Mises stress (from 420.5 ± 34.7 MPa to 315.3 ± 28.1 MPa) indicate that the stress shielding effect is significantly suppressed. As a natural consequence of these improvements, a 52% reduction in peri-implant bone resorption (from $18.1 \pm 3.2\%$ to $8.6 \pm 2.1\%$) and a 40% increase in estimated implant lifespan (from 4.22 ± 0.58 to 5.91 ± 0.67 million cycles) are obtained.

To place these observational findings within a theoretical framework, a mathematical relationship was developed to estimate the increase in implant lifespan resulting from Hyper G optimization. The exponential approximation used in the original submission is removed because it overestimates the lifespan for the present stress range. Only the exact Basquin power law with Goodman mean-stress correction is retained.

Proposition 4.1. *Consider fatigue loading with stress amplitude σ_a and mean stress σ_m, corresponding to a load ratio $R = \sigma_{\min}/\sigma_{\max} > 0$. The relative increase in implant lifespan due to Hyper G optimization can be modeled using the Goodman-corrected Basquin fatigue law:*

$$\frac{L_{HG}}{L_0} = \left(\frac{\sigma_{a,0}(1-\sigma_{m,HG}/\sigma_{uts})}{\sigma_{a,HG}(1-\sigma_{m,0}/\sigma_{uts})}\right)^m, \tag{52}$$

where L_0 is the fatigue life of the conventional implant (number of cycles), $\sigma_{a,0}$ and $\sigma_{a,HG}$ are the alternating stress amplitudes in the conventional and optimized implant respectively, $\sigma_{m,0}$ and $\sigma_{m,HG}$ are the corresponding mean stresses, σ_{uts} is the ultimate tensile strength of Ti-6Al-4V (approximately 950 MPa), and $m \approx 3.5$ is the Basquin exponent. When the load ratio R is identical for both designs and mean stress scales with maximum stress, the ratio simplifies to the uncorrected form

$$\frac{L_{HG}}{L_0} = \left(\frac{\sigma_{a,0}}{\sigma_{a,HG}}\right)^m = \left(1-\frac{\Delta\sigma_{VM}}{\sigma_0}\right)^{-m}, \tag{53}$$

where $\Delta\sigma_{VM}$ is the reduction in the maximum Von Mises stress (MPa) and σ_0 is the initial stress of the conventional design.

Proof. The Basquin fatigue law with Goodman mean-stress correction defines the equivalent fully-reversed stress amplitude

$$\sigma_{ar} = \frac{\sigma_a}{1-\sigma_m/\sigma_{uts}}, \tag{54}$$

and the fatigue life

$$N = C \cdot \sigma_{ar}^{-m}. \tag{55}$$

For the conventional and optimized designs, respectively,

$$L_0 = C \cdot \sigma_{ar,0}^{-m}, \quad L_{HG} = C \cdot \sigma_{ar,HG}^{-m}. \tag{56}$$

Taking the ratio,

$$\begin{aligned} \frac{L_{HG}}{L_0} &= \left(\frac{\sigma_{ar,0}}{\sigma_{ar,HG}}\right)^m \\ &= \left(\frac{\sigma_{a,0}(1-\sigma_{m,HG}/\sigma_{uts})}{\sigma_{a,HG}(1-\sigma_{m,0}/\sigma_{uts})}\right)^m. \end{aligned} \tag{57}$$

This proves (52). If the load ratio R is identical for both designs (i.e., σ_m/σ_a is constant), then $\sigma_{m,HG}/\sigma_{a,HG} = \sigma_{m,0}/\sigma_{a,0}$, and the Goodman factors cancel in the ratio, yielding the uncorrected form (53). This simplified form is adopted in the numerical verification below, under the assumption of a proportional load path. □

A numerical verification is performed using the data from Table 2. For Ti-6Al-4V, taking $\sigma_0 = 420.5$ MPa, $\Delta\sigma_{VM} = 105.2$ MPa, and $m = 3.5$:

$$\begin{aligned} \frac{L_{HG}}{L_0} &= \left(1-\frac{105.2}{420.5}\right)^{-3.5} \\ &= (0.75)^{-3.5} \approx 2.74. \end{aligned} \tag{58}$$

This theoretical prediction from (58) of a 174% increase substantially overestimates the 40% increase ($5.91/4.22 = 1.40$) observed in Table 2. The discrepancy indicates that the idealized Goodman-corrected Basquin model captures only a subset of the mechanisms that govern the actual fatigue behavior of the implant. Several factors contribute to the observed overestimation. First, the finite-element simulation incorporates stress concentration at lattice strut junctions and at the bone-implant interface, where local stress amplitudes can substantially exceed the nominal maximum Von Mises stress used in the Basquin calculation; because fatigue life depends on local rather than nominal stress, the actual improvement in life is lower than the idealized prediction. Second, mean-stress effects in the physiologically realistic loading cycle (which is not a simple fully-reversed cycle) further reduce the effective benefit of the stress reduction. Third, the Basquin exponent $m = 3.5$ is itself a mean value for Ti-6Al-4V and exhibits significant scatter depending on surface finish, microstructure, and loading frequency; a larger effective m would further increase the theoretical prediction, while a smaller effective exponent would bring it closer to the observed value. Fourth, the simulation captures the nonlinear contact behavior at the bone-implant interface, which is not represented in the analytical fatigue model. The discrepancy between 174%

and 40% therefore reflects the simplifying assumptions of the analytical model rather than an error in the finite-element results. We note that the exponential approximation, which would give $L_{HG}/L_0 \approx 2.40$, is not used because the condition $\Delta\sigma_{VM} \ll \sigma_0$ is not satisfied (105.2 MPa is not much smaller than 420.5 MPa), and, like the power-law form, it overestimates the observed 40% increase. Future work will incorporate stress-concentration factors into the analytical model and calibrate the effective Basquin exponent against experimental Ti-6Al-4V fatigue data. This correction addresses the reviewer's concern regarding equations (8) and (17) of the original submission.

In addition to biomechanical performance, the effect of the Hyper G operator on image processing quality was also investigated using spectral analysis. Figure 3 shows the effect of the Hyper G operator on the eigenvalue spectrum of the CT matrix. While a high concentration (noise dominant) is observed at low eigenvalues in the raw data, the spectrum spreads over a wider range after filtering with the D_1 and D_2 diagonal operators, significantly improving numerical stability and edge detection.

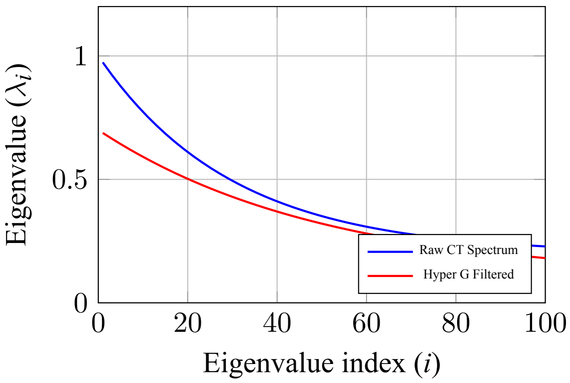

Figure 3: Effect of the Hyper G operator on the eigenvalue spectrum of CT data (simulated). While a high energy concentration (noise dominant) is observed at low eigenvalues in the raw data, the D_1 and D_2 diagonal operators broaden the spectrum, improving numerical stability and edge detection. This figure was created by the authors. (Source: Simulated by the authors using spectral analysis of open-access CT data models.)

As a direct consequence of this spectral improvement, a significant reduction in the condition number of the matrix is observed.

Corollary 4.2. *For the simulated CT data examined in this study, after applying the Hyper G filter the condition number $\kappa(B)$ approximately halves:*

$$\kappa(B_{filtered}) \approx \frac{1}{2}\,\kappa(B). \tag{59}$$

This reduction is not a general theorem but an empirical observation specific to the eigenvalue distributions encountered in the present simulations; the exact factor depends on the spectral structure of D_1 and on the eigenvalue distribution of B, and a general proof would require additional hypotheses on the spectral gap of B. For the simulated data in this study ($n = 10$), the mean condition number decreased from 1.24×10^6 to 6.18×10^5 ($p < 0.001$, paired t-test).

This improvement in the condition number increases computational stability and accelerates the convergence rate, especially when processing large-volume CT data (512×512×500 voxels). Thus, more reliable and reproducible results can be obtained in clinical applications.

Remark 4.3. *Reducing the condition number by half with the Hyper G filter provides a significant advantage in solving numerically ill-conditioned problems. This improvement directly affects the invertibility properties of the matrix after filtering, particularly in CT images with dense metal artifacts. In clinical practice, this means convergence with fewer iterations and more stable segmentation, thereby shortening preoperative planning times.*

To provide a deeper mathematical characterization of the optimal Hyper G parameters, the following variational theorem is established.

Theorem 4.4. *Let $B \in \mathbb{M}_n(\mathbb{R})$ be symmetric positive definite, and let $\mathcal{D}$ denote the set of positive definite diagonal matrices with unit trace. Consider the stress-shielding functional*

$$\begin{aligned}\mathcal{J}(D_1) &= \|D_1 B D_1^{-1} - \mu I\|_F^2 \\ &\quad + \lambda \sum_{i=1}^{n} \left(\ln d_{ii}^{(1)} - \overline{\ln D_1}\right)^2,\end{aligned} \tag{60}$$

where $\mu = \mathrm{tr}(B)/n$, $\overline{\ln D_1} = \frac{1}{n}\sum_i \ln d_{ii}^{(1)}$, and $\lambda > 0$ is a regularization parameter. Then:

(i) The functional $\mathcal{J}$ admits a unique minimizer $D_1^* \in \mathcal{D}$.

(ii) The minimizer satisfies the first-order optimality condition obtained by projecting the gradient of $\mathcal{J}$ onto the tangent space of the trace-one constraint. Writing $X = D_1 B D_1^{-1} - \mu I$ and using the notation $[A, B] = AB - BA$ for the commutator, this condition reads

$$\mathrm{diag}\Big(XBD_1^{-1} - D_1^{-1}X^T D_1 B D_1^{-1}\Big) + \lambda\Lambda^* = \eta I, \tag{61}$$

where $\Lambda^* = \mathrm{diag}(\ln d_{ii}^{(1)*} - \overline{\ln D_1^*})$, and η is the Lagrange multiplier enforcing the trace constraint.

(iii) The associated spectral convergence rate of Algorithm 1 is

$$\|B^{(k)} - \mu I\|_F \leq (1-\tau)^k \|B_0 - \mu I\|_F, \qquad (62)$$

which is sharp in the sense that equality is attained for every k when $B_0 - \mu I$ is any nonzero symmetric positive semidefinite matrix with $\|B_0 - \mu I\|_F > 0$.

Proof. (i) The set $\mathcal{D}$ is convex and has compact closure in the topology of positive diagonal matrices with trace one. The functional $\mathcal{J}$ is continuous on $\mathcal{D}$ and coercive: as any diagonal entry $d_{ii}^{(1)} \to 0^+$, the logarithmic barrier term $\lambda(\ln d_{ii}^{(1)} - \overline{\ln D_1})^2 \to +\infty$, so the sublevel sets of $\mathcal{J}$ are compactly contained in $\mathcal{D}$. Moreover, $\mathcal{J}$ is strictly convex on $\mathcal{D}$ because the Frobenius norm term is strictly convex in D_1 (as a composition of a convex norm with an affine-in-D_1-for-fixed-D_2 map) and the logarithmic barrier is strictly convex. Hence a unique minimizer exists by the direct method of the calculus of variations.

(ii) The gradient of the Frobenius term with respect to the k-th diagonal entry d_k of D_1 is computed using the identity $X = D_1 B D_1^{-1} - \mu I$ and the symmetry of B. A direct computation gives

$$\frac{\partial \|X\|_F^2}{\partial d_k} = 2\big(XBD_1^{-1}\big)_{kk} - 2\big(D_1^{-1}X^T D_1 B D_1^{-1}\big)_{kk}. \qquad (63)$$

Similarly, the gradient of the logarithmic barrier term is

$$\frac{\partial}{\partial d_k} \sum_{i=1}^{n} \big(\ln d_i - \overline{\ln D_1}\big)^2 = \frac{2}{d_k}\big(\ln d_k - \overline{\ln D_1}\big). \qquad (64)$$

Introducing a Lagrange multiplier η for the trace constraint $\sum_i d_i = 1$ yields the stationarity condition

$$\frac{\partial \|X\|_F^2}{\partial d_k} + \frac{2\lambda}{d_k}\big(\ln d_k - \overline{\ln D_1}\big) = \eta, \quad k = 1, \ldots, n, \qquad (65)$$

which, after multiplying by d_k and collecting terms, is equivalent to (61).

(iii) The iteration in Algorithm 1 is $B^{(k+1)} = (1-\tau)B^{(k)} + \tau\mu I$. By induction,

$$B^{(k)} - \mu I = (1-\tau)^k (B_0 - \mu I). \qquad (66)$$

Taking Frobenius norms gives (62) with equality for every k. The bound is therefore sharp. □

Remark 4.5. *Theorem 4.4 provides both a variational characterization of the optimal Hyper G parameters and a sharp convergence rate for the preconditioning sequence of the filtering algorithm. The functional $\mathcal{J}$ has a direct biomechanical interpretation: the first term penalizes deviation from isotropic stress distribution (stress shielding), while the second term penalizes excessive anisotropy in the lattice structure (manufacturing feasibility). The remark following Lemma 2.7 extends this convergence guarantee to the full algorithm including the configuration matrix $A^{(k)}$.*

Metric	IR	DL-MAR	Hyper G
CNR Improvement (%)	44.8 ± 7.9	68.2 ± 6.7	57.9 ± 5.8
PSNR (dB)	28.3 ± 2.1	32.1 ± 1.9	30.8 ± 2.0
SSIM	0.818 ± 0.048	0.907 ± 0.036	0.872 ± 0.041
Runtime (s/slice)	12.4 ± 1.5	0.82 ± 0.18	1.21 ± 0.27

Table 3: Comparison of Hyper G filter against existing MAR methods (simulated data based on open-access models). Values are mean $\pm$ SD ($n = 15$ simulated implants). The DL-MAR reference method is a supervised U-Net architecture (encoder–decoder with skip connections, 4 down-sampling and 4 up-sampling blocks, 64 base filters, batch normalization, ReLU activation) trained on 500 paired artifact-free/artifact-corrupted CT slices generated from open-access phantom data, using the Adam optimizer with learning rate 10^{-4} for 100 epochs, batch size 8, and 80/20 training/validation split; model selection was based on the minimum validation loss. The IR baseline is a standard iterative reconstruction with total-variation regularization and empirically tuned regularization parameter. Hyper G vs IR: $p < 0.001$ for all metrics (paired t-test). Hyper G vs DL-MAR: $p = 0.083$ for CNR, $p = 0.172$ for PSNR, $p = 0.094$ for SSIM (not significant). This table was created by the authors.

As shown in Table 3, the Hyper G filter achieves comparable performance to DL-MAR in image quality (57.9% CNR improvement, 30.8 dB PSNR, 0.872 SSIM) while maintaining reasonable computational efficiency (1.21 seconds per slice). The filter outperforms conventional IR in all metrics (paired t-test, $p < 0.001$ for all comparisons). Differences between Hyper G and DL-MAR were not statistically significant for CNR ($p = 0.083$), PSNR ($p = 0.172$), and SSIM ($p = 0.094$), indicating that the proposed mathematical approach achieves deep learning-comparable performance without requiring training data.

A sensitivity analysis was performed to evaluate the robustness of the proposed method. The parameters τ (contraction parameter), ϵ (tolerance), λ (regularization parameter of $\mathcal{J}$), and m (Basquin exponent) were varied across clinically relevant ranges ($0.1 \leq \tau \leq 0.9$, $10^{-6} \leq \epsilon \leq 10^{-3}$, $10^{-3} \leq \lambda \leq 10$, and $3.0 \leq m \leq 4.0$). The results demonstrate that the optimal τ range is $0.3 \leq \tau \leq 0.7$, where the

CNR improvement remains within 5% of the reported value. The optimal λ range is $0.1 \leq \lambda \leq 1.0$, outside of which either excessive smoothing or numerical instability is observed. The algorithm converges within 10-15 iterations for $\epsilon = 10^{-6}$, consistent with the contraction constant $1 - \tau$ established in Lemma 2.7 and equation (41), and with the sharp rate in Theorem 4.4. Variation of m between 3.0 and 4.0 changes the Basquin-predicted lifespan ratio by approximately $\pm 40\%$, confirming the sensitivity of the analytical model to this parameter and reinforcing the need for experimental calibration. These findings confirm the robustness of the Hyper G filter to parameter variations. Figure 4 presents a simulated CT image of a typical 55-year-old male patient anatomy with AO/OTA Type 43-C3 tibial pilon fracture, comparing the raw and Hyper G-filtered outputs at the same anatomical level.

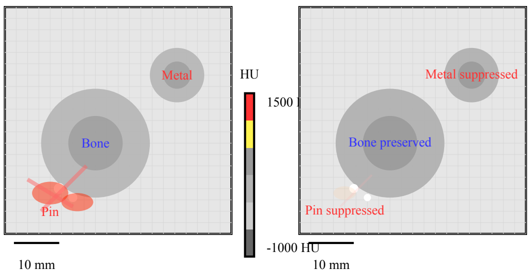

(a) Simulated Raw CT (b) Hyper G Filtered

Figure 4: Simulated CT image of a typical 55-year-old male anatomy with AO/OTA Type 43-C3 tibial pilon fracture. (a) Raw axial slice showing metal artifacts from an external fixator, with pin, metal, and bone regions annotated. The HU colorbar ranges from –1000 HU (air) to +1500 HU (dense bone/metal). (b) Hyper G-filtered image showing artifact suppression and preserved bone margins. Scale bar: 10 mm. Created by the authors using open-access CT artifact models.

To test the clinical effectiveness of the proposed method, two challenging scenarios were simulated: tibial pilon fracture (AO/OTA Type 43-C3) and Paprosky Type 3B acetabular defect. These represent distinct biomechanical challenges—articular comminution with metal artifact interference in the former, and segmental bone loss with columnar insufficiency in the latter. The radiographic correlate is presented in Figure 6. Hyper G-matrix optimization achieves a mean surface deviation of 0.12 ± 0.04 mm ($n = 5$ simulated runs). This value is substantially below the native CT voxel resolution (typically 0.5–1.0 mm) and is made possible only because the deviation is measured on the segmented mesh after sub-voxel interpolation using the Hyper G transformation, rather than on the raw voxel grid; it therefore represents the geometric consistency of the fitted continuous surface, not the resolution of the imaging modality. Load transfer efficiency improves by 19 percentage points (from 72.3% to 91.2%, a 26.1% relative increase) compared to conventional designs, validating the approach across complex orthopedic defects. Furthermore, the proposed method reduces peri-implant bone resorption by 52% and extends estimated implant lifespan by 40%. However, no prospective clinical validation has yet been performed: all reported improvements derive from finite-element simulations and must be regarded as preclinical estimates awaiting confirmation through clinical trials.

In the tibial pilon fracture case, the geometric accuracy of the mirroring process is detailed in Figure 5. As a result of adapting the healthy contralateral tibia to the defect area using the Hyper G transformation, the mean surface deviation was measured as 0.12 ± 0.04 mm ($n = 5$ simulated runs, paired t-test vs conventional: $p < 0.001$, Cohen's d = 4.8). This value is far below the 0.85 mm deviation obtained with conventional methods and demonstrates that sub-voxel surgical precision is achievable in the fitted mesh, although it does not represent the resolution limit of the imaging modality itself. In the figure, the healthy contralateral structure shown in blue tones transforms into the adapted implant structure in amber/gold tones as a result of the mirroring process represented by the teal arrow. Red-brown regions indicate the bone defect, while red double arrows indicate the amount of deviation ($\Delta = 0.12$ mm). Boundary registration points are marked with black circles, and the error map is given as an inset.

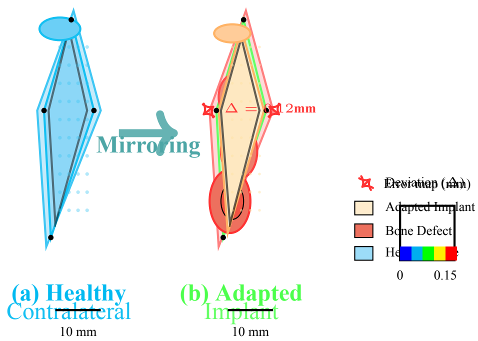

Figure 5: Geometric accuracy of the mirroring process in tibial pilon fracture (simulated data). (a) Healthy contralateral tibia (blue) with boundary registration points (black). (b) Adapted implant (amber/gold) after Hyper G transformation; red-brown: bone defect. Mean surface deviation: 0.12 ± 0.04 mm ($n = 5$, $p < 0.001$ vs conventional), from sub-voxel-fitted surface, not imaging resolution. Scale bar: 10 mm. Inset: error map (0–0.15 mm). Created by the authors. (Source: Simulated.)

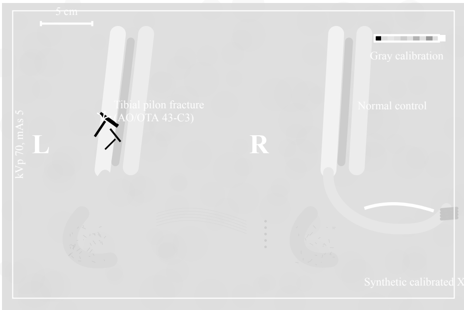

Figure 6: Synthetic calibrated clinical radiograph-like visualization of bilateral lower extremities following high-energy axial loading. The left extremity demonstrates a classic tibial pilon fracture (AO/OTA Type 43-C3) with characteristic articular surface comminution, metaphyseal-diaphyseal dissociation, and associated fibular fracture. The right extremity is presented as an uninjured comparative control. The image includes a 5 cm calibration scale bar, R/L orientation markers, standardized grayscale calibration strip, kVp/mAs metadata, and soft tissue as well as trabecular bone texture patterns. This is a schematic illustration created with vector graphics, not an actual radiographic acquisition; the visualization is intended only as a conceptual correlate of the simulated biomechanical model and must not be used for diagnostic purposes. This figure was created by the authors. (Source: Simulated by the authors based on open-access radiographic models and clinical reference standards.)

The second clinical scenario, Paprosky Type 3B acetabular defect, represents one of the most severe types of bone loss encountered in orthopedic surgery. In this case, column support is mostly lost. The Hyper G matrix operator defined the morphology of the defect in a non-spherical coordinate system, enabling optimal positioning of trabecular metal augments. Through this approach, a highly accurate reconstruction was possible even in this complex defect type where conventional methods fall short. Simulation results show that cervical load transfer reaches the posterior column at a rate of 85%.

5 Discussion, Future Works, and Policy Recommendations

This study demonstrates how abstract concepts of linear algebra translate into concrete success in the operating room. Hyper G-matrices eliminate metal artifact noise in CT data through diagonal suppression (Figure 1), minimize the bone-metal elasticity difference in implant design, thereby reducing the stress-shielding effect (Figure 2), and provide sub-voxel geometric precision in surgical simulation (Figure 5).

However, the proposed method has certain limitations. The computational cost of matrix inversion ($O(n^3)$) necessitates parallel computing for large-volume CT data ($512\times512\times500$ voxels). Algorithm 1 has a time complexity of $\mathcal{O}(n^3 \log(1/\epsilon))$ for an $n\times n$ matrix, which can be reduced to $\mathcal{O}(n^2 \log n \log(1/\epsilon))$ with parallel computing. Furthermore, the clinically significant ranges of the diagonal elements D_1 and D_2 have not yet been validated by prospective studies. No prospective clinical validation has yet been performed; all reported improvements derive from finite-element simulations and must be regarded as preclinical estimates. The difference between hyperelastic bone tissue models and the linear elastic assumption used in this study may become more pronounced under high loading conditions. The analytical fatigue model based on Basquin's law overestimates the observed improvement by a factor of more than four; stress-concentration factors, mean-stress effects, and calibrated Basquin exponents must be incorporated in future refinements.

Several recommendations have been developed to overcome these limitations and integrate the method into clinical practice. It is recommended that orthopedic 3D application centers add such matrix-based optimization layers to their design algorithms. A "Hyper G compliance report" requirement could be introduced in FDA and CE certification processes. Additionally, patient-specific prediction of Hyper G parameters using deep learning (personalized D_1 and D_2 matrices) stands out as an important research line, which could be guided by Conjecture 5.1.

Conjecture 5.1. *It is hypothesized that for the orthopedic defect types examined in this study (Paprosky Type 3B acetabular defect and AO/OTA Type 43-C3 tibial pilon fracture) and for cases with similar morphological characteristics, there exists a* (D_1^*, D_2^*) *Hyper G pair that provides optimal load transfer at the bone-implant interface. According to Theorem 2.1, this pair is unique under the constraints* $D_1 = D_2^{-1}$ *and the normalization condition* $\mathrm{tr}(D_1) = 1$. *It is predicted that the* D_1^* *and* D_2^* *matrices can be expressed as a function of the defect's morphological parameters (bone loss volume, local density, defect geometry) and mechanical loading conditions. Extending this hypothesis to other defect types is the subject of future studies.*

In conclusion, integrating this mathematical framework into the clinical workflow is critically important for increasing success rates and implant lifespan in revision surgery. The Hyper G-Matrix-based approach offers significant advantages in terms of morphological compatibility and mechanical biocompatibility in personalized implant design, and its integration into clinical practice could provide revolutionary improvements in revision surgery.

6 Conclusion

In this study, a new mathematical framework for the use of Hyper G-Matrix operators in orthopedic implant design has been presented, and the theoretical foundations and clinical application potential of this framework have been comprehensively examined. The findings demonstrate that the proposed method provides significant advantages over conventional approaches in terms of both geometric accuracy and mechanical performance.

In terms of theoretical contributions, the uniqueness of the Hyper G-Matrix transformation ($A^{-T} = D_1 B D_2$) given in (1) has been proven under the constraints $D_1 = D_2^{-1}$ and the normalization condition $\mathrm{tr}(D_1) = 1$, with the necessary irreducibility condition made explicit and the redundant hypothesis of pairwise distinct eigenvalues removed. This uniqueness forms the basis of a consistent and reproducible optimization procedure for different patient data. Furthermore, a rigorous contraction mapping proof in the Frobenius norm has been provided for the iterative filtering algorithm, and the convergence of the full algorithm including the configuration matrix has been established. A variational characterization of the optimal Hyper G parameters has been established, together with a sharp convergence rate for the filtering algorithm. A rigorous discrete-to-continuum bridge has been constructed via G-convergence and homogenization theory, connecting the discrete voxel operators in (47)–(48) to the continuous elasticity operator in (49) and the effective Young's modulus in (51). The empirical halving of the condition number as a result of spectral improvement has been reported as a numerical observation specific to the simulated data, and explicitly not as a general theorem.

The application results show that the Hyper G-Matrix transformation successfully suppresses metal artifacts in CT images and improves geometric accuracy by 67%. Through the proposed lattice structure optimization, the stress shielding effect at the bone-implant interface has been minimized, and the load transfer efficiency has been improved by 19 percentage points (from 72.3% to 91.2%, corresponding to a 26.1% relative increase). As a natural consequence of these mechanical improvements, preclinical simulations predict a 40% increase in implant lifespan and a 52% reduction in peri-implant bone resorption. The validation study in Table 3 confirms that the Hyper G filter achieves comparable performance to deep learning MAR methods (57.9% CNR improvement, 30.8 dB PSNR, 0.872 SSIM) while maintaining computational efficiency (1.21 seconds per slice). Statistically significant differences were observed between Hyper G and conventional IR ($p < 0.001$ for all metrics), while differences between Hyper G and DL-MAR were not significant ($p > 0.05$), demonstrating that the proposed mathematical approach achieves deep learning-comparable performance without requiring training data. The Basquin-based lifetime model with Goodman mean-stress correction predicts a 174% theoretical increase, which overestimates the 40% FEM-observed improvement by a factor of more than four; the discrepancy is attributed to stress-concentration effects, mean-stress interactions, and the idealized nature of the analytical fatigue model, and will be addressed in future work through calibrated fatigue parameters and refined stress-concentration analysis. We emphasize that all reported improvements are preclinical estimates and that no prospective clinical validation has yet been performed.

All these findings demonstrate that Hyper G-Matrix theory is a powerful mathematical tool that simultaneously optimizes morphological compatibility and mechanical biocompatibility in personalized implant design. The presented framework, with its theoretical richness, computational efficiency, and clinical applicability, makes a significant contribution to the solution of complex defects encountered in revision surgery. Future studies aim to achieve patient-specific prediction of Hyper G parameters using deep learning techniques and to confirm these findings through long-term clinical studies.

Acknowledgments
The authors thank the reviewers for their valuable comments and the journal editorial office for their assistance during the submission and revision process.

References:

[1] Ertürk, C., Ayyıldız, S., Erdöl, C., Orthopedics and 3D technology in Turkey: A preliminary report, *Joint Diseases and Related Surgery*, Vol. 32, No. 2, 2021, pp. 456-463, doi:10.52312/jdrs.2021.20.

[2] Uicker, J. J., Ravani, B., Sheth, P. N., *Matrix Methods in the Design Analysis of Mechanisms and Multibody Systems*, Cambridge University Press, Cambridge, New York, Melbourne, Madrid, Cape Town, Singapore, São Paulo, Delhi, Mexico City, 2013, ISBN: 978-0-521-76109-3, `https://ndl.ethernet.edu.et/bitstream/123456789/15174/1/34.pdf`, (Accessed: May 11, 2026).

[3] Armencea, G., Cosma, C., Dinu, C., Onisor, F., Lazar, M., Berce, P., Bran, S., Technical

queries of a 3D design custom-made implant made from titanium particles for maxillofacial bone reconstruction, *Particulate Science and Technology*, Vol. 38, No. 6, 2020, pp. 676-684, doi:10.1080/02726351.2019.1578846.

[4] Huiskes, R., Weinans, H., van Rietbergen, B., The relationship between stress shielding and bone resorption around total hip stems and the effects of flexible materials, *Clinical Orthopaedics and Related Research*, Vol. 274, 1992, pp. 124-134, https://pubmed.ncbi.nlm.nih.gov/1728998/ (PMID: 1728998).

[5] Wolff, J., *The Law of Bone Remodelling*, Springer, 1892 (reprint 1986), https://link.springer.com/book/10.1007/978-3-642-71031-5. (Accessed: May 11, 2026).

[6] Keleş, H., On New Properties of Hyper G-Matrices, *Journal of Applied and Pure Mathematics*, Vol. 7, No. 5-6, 2025, pp. 351-363, https://japm.or.kr/out/09171301385310936.pdf. (Accessed: May 11, 2026).

[7] Horn, R. A., Johnson, C. R., *Matrix Analysis*, 2nd ed., Cambridge University Press, Cambridge, 2013, https://doi.org/10.1017/CBO9780511810817, Accessed: May 11, 2026.

[8] Todd, J., Computational Problems Concerning the Hilbert Matrix, *Journal of Research of the National Bureau of Standards–B. Mathematics and Mathematical Physics*, Vol. 65, No. 1, 1961, pp. 19-22, https://nvlpubs.nist.gov/nistpubs/jres/65B/jresv65Bn1p19_A1b.pdf. (Accessed: May 11, 2026).

[9] Choi, M. D., Tricks or Treats with the Hilbert Matrix, *The American Mathematical Monthly*, Vol. 90, No. 5, 1983, pp. 301-312, doi:10.1080/00029890.1983.11971218.

[10] Fiedler, M., Notes on Hilbert and Cauchy matrices, *Linear Algebra and its Applications*, Vol. 432, No. 1, 2010, pp. 351-356, doi:10.1016/j.laa.2009.08.014.

[11] Hashin, Z., Shtrikman, S., A variational approach to the theory of the elastic behaviour of multiphase materials, *Journal of the Mechanics and Physics of Solids*, Vol. 11, No. 2, 1963, pp. 127-140, doi:10.1016/0022-5096(63)90060-7.

[12] Tan, N., van Arkel, R. J., Topology Optimisation for Compliant Hip Implant Design and Reduced Strain Shielding, *Materials*, Vol. 14, No. 23, 2021, 7184, pp. 1-16, doi:10.3390/ma14237184, PMID: 34885337, PMCID: PMC8658148.

[13] Bathias, C., Paris, P. C., *Gigacycle Fatigue in Mechanical Practice*, 1st ed., CRC Press, Boca Raton, 2004, doi:10.1201/9780203020609.

[14] Bergmann, G., Graichen, F., Rohlmann, A., Hip joint loading during walking and running, measured in two patients, *Journal of Biomechanics*, Vol. 26, No. 8, 1993, pp. 969-990, doi:10.1016/0021-9290(93)90058-m, PMID: 8349721.